Tumor Spheroids Layered in an Imageable Cancer Environment (T-SLICE): a novel *in vitro* platform to study tumor biology

Morgan Pugh-Toole[1,2]¶, Nicholas Dawe [2,3]¶, Andrew Smith[3], Jeanette E. Boudreau[1,2,4], Brendan M. Leung*[1,2,3,5]

[1]Department of Pathology, Dalhousie University

[2]Beatrice Hunter Cancer Research Institute, Dalhousie University

[3]School of Biomedical Engineering, Dalhousie University

[4]Department of Microbiology & Immunology, Dalhousie University

[5]Department of Applied Oral Sciences, Dalhousie University

Mailing Address: 5891 University Avenue, Dentistry Building, Room 5193, Halifax NS, B3H 1W2

*Corresponding author

Email: bleung@dal.ca

¶ These authors contributed equally to this work

Abstract:

Cancer treatment is shifting towards precise medicine informed by tumor genetics and structural features. In recent years, it has become increasingly recognized that patient tumors—even those of the same tissue origin—can differ substantially between patients and respond differently to treatment. Given this, it is necessary to design therapies that target the heterogeneity of tumors. When investigating novel therapeutics in the laboratory, conventional cell culture models do not adequately recapitulate this heterogeneity and therefore may not accurately represent drug responses. Recent advances in miniaturized organ-on-a-chip models have been able to generate more complex microenvironments for *in vitro* studies. However, many of these models do not resemble the scale of clinically relevant tumors and pose a high barrier to use because they are technically complex. To facilitate mechanistic studies of the tumor microenvironment (TME), we designed T-SLICE, a chip made using commercially available elastomers and designed to fit in a standard 6-well plate. This simple 3-D tumor model incorporates microfluidic principles into a fully customizable TME, wherein cells drive the formation of biochemical gradients akin to those observed within a real tumor. In T-SLICE, spheroids are seeded atop a monolayer of fibroblasts situated between two closely spaced coverslips (300-700 μm). The restrictive gap height limits the permeation of oxygen (O_2) and hinders the removal of carbon dioxide (CO_2) and metabolic waste, which leads to the generation of tumor-like hypoxic gradients. We demonstrate that T-SLICE establishes cell-driven oxygen gradients leading to the formation of a hypoxic core, with further impacts on cellular viability, mitochondrial membrane potential (MMP), and proliferation. T-SLICE cultures can be imaged live or fixed and stained for immunohistochemistry (IHC). These features of T-SLICE make it an accessible and faithful model of a tumor's heterogeneity and open the possibility for more faithful testing of novel therapeutics in the context of a realistic TME.

41 **Introduction**

42 Tumors are dynamic networks of tumor and stromal cells that together form a microenvironment
43 with gradients of nutrients and oxygen[1]. Within the tumor microenvironment (TME) across various
44 cancer histologies, the relative compositions of stromal and tumor cells vary, with impacts on
45 tumor biochemistry, prognosis, and response to treatment[2]. The TME is highly dynamic and
46 diverse, and biochemical factors within the TME allow cancer cells to persist and metastasize into
47 healthy tissues. There are many different modes of studying the TME in 2-D or 3-D formats,
48 however many existing models fall short of faithfully recapitulating these complexities[1, 3]. The
49 emergence of microfluidic tumor models has allowed for the recapitulation of some tumor
50 biochemistry; however, these are often complex and out of reach for cancer biology laboratories,
51 and thus not implemented for cancer research[4-6]. In this work, we set out to create a simple,
52 accessible, yet representative 3-D culture system that could be used to study the TME, and
53 ultimately better inform its biology and the development of cancer therapies.

54 In tumors, hypoxia (low oxygen) is common at the tumor's center as cancer growth
55 outpaces vascularization[7-10] . Acute and chronic hypoxic responses lead to the accumulation of
56 reactive oxygen species (ROS) that can drive DNA damage and apoptosis in healthy cells[10]. Over
57 time, the accumulation of irreparable DNA mutations gives rise to apoptosis resistance and
58 advancing malignancies[11]. The rapid proliferation of cancer cells makes them metabolically
59 demanding; this generates biochemical gradients that vary with tumor size, blood supply, and
60 composition[12, 13]. Without sufficient mechanisms for nutrient delivery and waste clearance,
61 compounded by hypoxia, cells at the tumor's core evolve differently from those at its periphery.
62 Tumor cells adapt, with manifestations of decreased proliferation and oxidative respiration,
63 increased accumulation of mutations and ROS, and resistance to apoptosis[14, 15]. These layers of

64 biochemical and tumoral diversity drive the selection of subsets of cancer cells that may confer
65 resistance to treatment[14].

66 Promising preclinical pharmaceutical and immunotherapy candidates demonstrate a low
67 success rate in phase III clinical trials, with a cumulative failure rate of approximately 97%[16, 17].
68 Likely, these studies reflect that most tumors are only partially sensitive to therapeutic
69 interventions because their heterogeneity is underrepresented in existing preclinical models. Over
70 the past two decades, the applications of microfluidic technologies within microscale models have
71 allowed for *in vitro* simulation of crucial biophysical features of solid tumors including chemical
72 gradients, matrix stiffness, hydrodynamic fluid flow, and mechanical stresses [18]. Various iterations
73 of channel[19] and multilayer[20] microfluidic devices allow for the precise arrangement of tumor,
74 stromal and immune cells within a defined microenvironment, while simultaneously imposing
75 biochemical gradients. Moreover, the biochemical gradients driven by cell metabolism within
76 diffusion-limiting microfluidic designs allow the development of a hypoxic core as established by
77 cells within native tumors[21]. This was recently demonstrated in a channel-based microfluidic
78 device with a thin gap culture chamber[22]. This model demonstrated the establishment of a hypoxic
79 core driven by cell metabolism, with consequences on chemotherapy sensitivity as a function of
80 oxygen tension[22].

81 This demonstrates that these next-generation microfluidics may be better equipped to inform
82 treatments of complex tumors.

83 The widespread adoption of microfluidic models for cancer therapy testing is hindered by
84 the accessibility of these devices to biology laboratories. For example, the reliance on hydrophilic
85 capillary forces to passively load cells into gradient-based microfluidics necessitates plasma or
86 chemical activation and fundamentally limits the size of the device (and hence the tumor that can

87 be modelled). In pre-assembled devices, pre-bonding of the device before cell loading eliminates
88 the possibility of depositing cells, extracellular matrices and reagents in designated patterns with
89 bioprinting techniques, so their spatial organization cannot be controlled. The arrangement,
90 proximity and communication between cells each predicts tumor progression[23, 24], so conventional
91 pre-bonded microfluidic devices with closed channels cannot fully recapitulate important
92 histological aspects of tumors[25, 26].
93 To enable high-content and mechanistic studies that recapitulate the TME, we created Tumor
94 Spheroids Layered in an Imageable Cancer Environment (T-SLICE). T-SLICE incorporates
95 principles of microfluidic design, is compatible with standard biology laboratories, and has tunable
96 biochemical and cellular parameters that recreate features of the TME while remaining fully
97 imageable. In T-SLICE, small spheroids (<100 cells) are seeded atop a fibroblast monolayer which
98 is situated between two glass coverslips with a narrow vertical gap height (300-700 μm). The small
99 gap space minimizes convective transport caused by bulk fluid flow, creating a diffusional
100 resistance that is inversely proportional to its height. Within T-SLICE, cells situated closer to the
101 edge of the parallel glass coverslips preferentially receive oxygen and nutrients. The arrangement
102 of spheroids and fibroblasts within T-SLICE creates the topography, cellularity, and
103 dimensionality characteristic of real tumors. The spheroids are small enough that intra-spheroid
104 gradients are negligible, and the imageability limit of conventional spheroid culture is overcome
105 by uncoupling tissue architecture from metabolically generated biochemical gradients. By
106 enabling control of biochemical gradients independently from tumor tissue density, T-SLICE
107 permits live cell imaging *in situ*, empowering high-content experiments to test therapeutic
108 interventions. We demonstrate that the steepness of the hypoxic gradient is inversely proportional
109 to the gap between the two coverslips and that with increasing exposure to hypoxia (i.e. proximity

110 to the center of the T-SLICE chip), cellular proliferation, viability and mitochondrial membrane
111 potential (MMP) decrease. Hence, in this simple model, into which cells, stroma and tumor cells
112 can be arrayed as desired by the investigator to represent specific aspects of tumor histology, the
113 hypoxic gradient and metabolic challenges with which it is associated are created. We thereby
114 expect that T-SLICE will enable research that is better predictive of interactions and therapeutic
115 responses in real tumors, accelerating the development of new treatments toward clinical trials.
116

117 **Materials & Methods**

118 **3-D mold design and printing**

119 T-SLICE design and construction are depicted in **Figs 1A, and 1B**. T-SLICE chips were designed
120 using Autodesk® Fusion 360™ Computer-Aided Design (CAD) software as '.stl' files, then
121 converted to '.ctb' files using Chitubox® 3-D printing preprocessing software. Designs were 3-D
122 printed using an ELEGOO Mars 2 Pro MSLA 3-D Printer (ELEGOO, Shenzhen. China). Molds
123 were created from Standard LCD UV-Curing Photopolymer Rapid Resin (ELEGOO, Shenzhen.
124 China) in 0.05mm layers, each cured by 6 seconds of UV light exposure (405nm). Resin molds
125 were washed in isopropanol (20 min) and UV-cured (405 nm, 30 min) (ELEGOO Mercury Plus
126 Washing and Curing Machine, Shenzhen. China). Uncured resin monomers were extracted from
127 molds by washing thrice in 95% ethanol for 24 h with agitation.

128 T-SLICE chips were prepared by pouring Polydimethylsiloxane (PDMS) (10:1 elastomer
129 to curing agent, Sylgard 184™ Silicone Elastomer Kit, Corning) into the resin molds, degassed in
130 a vacuum chamber for 15 min, then cured (60°C for 24h) and removed using forceps. An 18mm
131 circular glass coverslip was covalently bonded to the underside of the chip by plasma oxidation
132 (1-2 min). Before use in cell culture, T-SLICE chips were sterilized in 70% ethanol and exposed

133 to UV light for 30 min.

134

135 **Cell Culture**

136 The NIH/3T3 (fibroblast), MCF-7 and HCC1806 (breast cancer) cell lines were obtained from the
137 American Type Culture Collection (ATCC), and the ID8 *Trp53*$^{-/-}$ (murine ovarian cancer) cell line
138 was generously gifted by Dr. Madhuri Koti (Queen's University). Cells were maintained in a
139 humidified incubator at 37ºC and 5% CO_2. MCF-7 and NIH/3T3 cells were maintained Dulbecco's
140 Modified Eagle Media (DMEM; Gibco) supplemented with 10% fetal bovine serum (FBS; Gibco)
141 and 1% antibiotic-antimycotic (AA;100 IU/mL penicillin, 0.1 mg/mL streptomycin and 0.25
142 µg/mL amphotericin-B, Gibco,). HCC-1806 cells were maintained in RPMI-1640 media (Gibco)
143 supplemented with 10% FBS and 1% AA. ID8-*Trp53*$^{-/-}$ cells[12] were maintained in DMEM
144 supplemented with 10% FBS, 1% penicillin-streptomycin (PS; Wisent), and 1% Insulin
145 Transferrin Selenite (ITS; Wisent Bioproducts).

146

147 **Spheroid culture and T-SLICE assembly**

148 Tumor spheroids were formed using Perfecta3-D™ 384-well hanging drop culture plates (3-D
149 Biomatrix Inc. Ann Arbor, MI). Hanging drop plates were pretreated in 0.1% w/v Pluronic® F108
150 solution (Sigma-Aldrich) in distilled water, then rinsed with dH_2O and UV-sterilized for 30 min
151 prior to use. MCF-7 or HCC1806 and ID8-*Trp53-/-* were seeded in 25 µl droplets containing 50-
152 100 cells, supplemented with 2.4 mg/mL MethoCel® A4M (Sigma-Aldrich) to create spheroids
153 with diameters of <150 µM **(Fig 1C)**. To prevent spheroids from merging, droplets were seeded
154 in a lattice pattern, yielding 192 spheroids for each 384-well hanging drop plate. Spheroids were
155 maintained in standard cell culture conditions (37°C, 5% CO_2). Following spheroid formation (24h

156 for MCF-7; 48h for HCC1806 and ID8-*Trp53-/-*), spheroids were collected, centrifuged at 200 x
157 *g*, and resuspended in 500 μL cell culture media, which was then used to replace the culture media
158 atop the fibroblasts.

159 T-SLICE cultures were assembled in standard six-well cell culture plates. NIH/3T3
160 fibroblasts were cultured on autoclaved No. 1 18mm round coverslips (VWR) pretreated with
161 fibronectin (10 μg/mL in PBS; Sigma-Aldrich) **(Fig 1B)**. The pretreated coverslips were seeded
162 with NIH/3T3 fibroblasts overnight at 200,000 cells per coverslip (400,000 cells/mL) to reach
163 100% confluency, and then 192 spheroids were added dropwise to each coverslip. After overnight
164 co-culture of the fibroblasts and spheroids, the T-SLICE chip was placed on top of the coverslips,
165 and 2 mL of cell culture media was added at the sides of the T-SLICE chip to fill it by capillary
166 action. Media was partially exchanged by replacing 500mL every 24 h. Control wells of co-
167 cultures without T-SLICE chips were cultured in parallel to ascertain the impact of the chip on
168 cellular processes. Zones of T-SLICE were defined as middle, intermediate and peripheral zones,
169 representing concentric rings of 0-3 mm, 3-6 mm or 6-9 mm diameter, respectively.
170

171 **EF5 characterization of hypoxic responses**

172 To characterize hypoxic cellular responses, we cultured T-SLICE in the presence of 100 mM of
173 the EF5 Hypoxia Detection Kit according to the manufacturer's instructions (Sigma-Aldrich). EF5
174 (2-(2-Nitro-1H-imidazol-1-yl)-N(2,2,3,3,3-pentafluoropropyl) acetamide), is a 2-nitroimidazole
175 compound that is reduced in hypoxic cells to form adducts at the cell membrane that can be
176 fluorescently labelled with a fluorophore-conjugated anti-EF5 antibody[13]. Cell culture media was
177 supplemented with 100 μM EF5 and was replenished every 24 hours. Cultures were assessed at 6,
178 12, 24, or 48 h time points. After the T-SLICE chip was removed, cells were fixed in 4%

179 paraformaldehyde (PFA) in PBS overnight at 4°C in the dark. Cells were then washed and prepared
180 for imaging, using the anti-EF5 (clone ELK3-51-Cy3) at 5 mg/mL in 1% BSA/PBS (Sigma
181 Aldrich). Imaging was performed on the EVOS^{TM} FL Auto 2 Cell Imaging System, and analysis
182 was conducted using ImageJ. Imaging was completed using the EVOS^{TM} Light Cube, RFP 2.0
183 (Ex: 542 nm; Em: 593nm).

184 **Assessment of Cellular proliferation using EdU**

185 Cell proliferation in T-SLICE zones was analyzed using an EdU (5-ethynyl-2'-deoxyuridine) Cell
186 Proliferation Kit (Click-iT^{TM} EdU Cell Proliferation Kit for Imaging, Alexa Fluor^{TM} 488 dye:
187 Invitrogen). Cell culture media was supplemented with 10 mM EdU which was replenished every
188 24 h. After 72 h, T-SLICE chips were removed, and the cells were fixed with 4% PFA in PBS for
189 15 min at RT and then stained according to the manufacturer's instructions. Imaging was performed
190 using the EVOS^{TM} Light Cube, GFP 2.0 (Ex: 482nm; Em: 524nm).

191 **Assessment of cell viability using Calcein-AM and Ethidium homodimer-1**

192 Cell viability was assessed using Calcein-AM (ThermoFisher Scientific) to label live cells and
193 ethidium homodimer-1 (EthD; Invitrogen) to label dead cells. At specified timepoints, T-SLICE
194 chips were removed, and then cells were washed with PBS and stained with a PBS solution
195 containing 1 μM Calcein-AM and 1 μM ethidium homodimer-1 for 30 min at rt in the dark. Cells
196 were washed twice with PBS and imaged using the EVOS^{TM} Light Cube, GFP 2.0 (Ex: 482 nm,
197 Em: 524 nm) and EVOS^{TM} Light Cube, RFP 2.0 (Ex: 542 nm, Em: 593 nm).
198

199 **Mitochondrial Membrane Potential measurement with MitoView 633**

200 MitoView^{TM} 633 (Biotium) was used to measure mitochondrial membrane potential (MMP)

201 according to the manufacturer's recommendations. Cell culture media was supplemented with 100
202 nM MitoView 633 (Biotium) for the duration of T-SLICE culture. T-SLICE cultures were imaged
203 live every 24 h using the EVOS^{TM} Light Cube, Cy5 2.0 (Ex: 635 nm, Em: 692 nm).

204

205 **Statistical analysis**

206 Statistical analysis of data was performed using GraphPad Prism 9 (GraphPad Software). Two-
207 way analysis of variance (ANOVA) with Tukey's multiple comparisons test was performed to
208 assess multi-group comparisons and α was set to 0.05. *P*-values are represented as follows:
209 *$*p<0.05$; $**p<0.01$; $***p<0.001$; $****p<0.0001$.*

210

211 **Results**

212 **Conceptualization, design and development of T-SLICE.**
213 We sought to design a model that recapitulates the biochemical properties of the solid tumor
214 amenable to use in biology laboratories. We considered chip geometry, cell growth surface area,
215 and distance between the two parallel glass coverslips as variables that would influence
216 biochemical gradients. Mitochondrial health, cell proliferation and vitality are all linked to tumor
217 cell diversification and oxygen availability, so we prioritized the generation of hypoxia in our
218 design. We hypothesized that cellular metabolism by a co-culture of spheroids and stromal cells
219 would generate an oxygen gradient with a hypoxic core in a chip where diffusion of oxygen and
220 nutrients through the media would be restricted to the lateral plane. Other key features considered
221 in this iterative process included ease of use and compatibility with live cell imaging and endpoint
222 IHC.

223 Throughout the design process, we tested several prototypes, including different shapes

224 and sizes and elected to use a circular chip for its symmetry. We elected to assemble a chip that
225 was comprised of a standard 18 mm round coverslip bonded on the underside of a
226 polydimethylsiloxane (PDMS) chip of 24 mm diameter. Below the chip, a second 18 mm round
227 coverslip was situated onto which cells would be cultured.

228 We first conducted a series of simulations using COMSOL Multiphysics® v. 6.2.
229 (www.comsol.com, COMSOL AB, Stockholm, Sweden) to predict the range of heights that would
230 promote hypoxia and thus, the useful range of T-SLICE chip heights. We modelled the generation
231 of hypoxia as a function of time (**Fig 2A**), and at three gap heights (300, 500, 700 mm, **Fig 2B**),
232 predicting the radial O_2 concentration from the periphery to the center of T-SLICE (radius = 9
233 mm). We assumed the outer edge (peripheral) O_2 concentration to be 6.7 mg/L (0.21 mol/m^3),
234 which is the dissolved oxygen saturation in water at sea-level[10]. To predict how O_2 tension would
235 change from the periphery to the center of T-SLICE at 37°C and by metabolism of cells on the
236 bottom coverslip, we assumed that no O_2 diffusion was occurring through the top and bottom glass
237 layers, and set the bottom layer of the model as a surface reaction layer to simulate a constant
238 oxygen consumption rate per cell of 6 x 10^{-17} mol/cell/s, scaled to the average density of a confluent
239 cell monolayer (2.67x10^4 cells/cm^2). This resulted in an overall consumption rate of 1.6 x 10^{-8}
240 mol/(m^2 s) [27].

241 In our simulations, both time and gap height impacted the onset and degree of hypoxia. Over a
242 simulation period of 24h, the model showed that a steady state oxygen gradient was reached after
243 12 h in the 500 µm T-SLICE chip, where an anoxic core of 3 mm diameter was predicted in the
244 center (**Fig 2A**). The study was then repeated for T-SLICE with 300 µm and 700 µm gap heights.
245 Steady-state results (T= 12 h) predicted an increase in anoxic core diameter to 11.2 mm when the
246 gap height was reduced to 300 µm. Inversely, when the gap height is increased to 700 µm the

247 anoxic core is eliminated with a center minimum oxygen concentration equal to 0.0549 mol/m^3
248 (**Fig 2B**).

249 **Functional testing of the T-SLICE model**

250 To test the validity of our simulations and move toward a working T-SLICE model *in vitro*, we
251 assembled co-cultures of fibroblasts and spheroids under T-SLICE chips (**Figs 1A and 1B**).
252 Fibroblasts are one prominent cell type found in the TME of many tumors, therefore we chose to
253 incorporate them in T-SLICE to represent the stromal compartment of tumors. We used NIH/3T3
254 embryonic murine fibroblasts as the gradient-driving stromal monolayer in all T-SLICE co-
255 cultures described. The NIH/3T3 cells were grown to 100% confluency on 18 mm coverslips. Once
256 confluent, tumor spheroids derived from hanging drop culture were seeded on top of the fibroblast
257 monolayer. We tested a range of cell seeding densities and found that $2x10^5$ NIH/3T3 cells per
258 coverslip established a confluent monolayer in 24 h, onto which tumor spheroids could be
259 supported without direct contact with the coverslip and associated deformation due to spheroid
260 adhesion spreading **(Figs 1B and 1C)**. In parallel, we optimized cancer cell seeding densities in
261 hanging drop culture to create spheroids with a diameter <150 µm. We chose this limit to minimize
262 the generation of intra-spheroid biochemical gradients and to ensure that the oxygen availability
263 to the spheroid is dependent only on its position under the T-SLICE chip. The small size of the
264 spheroid further allows microscopic imageability and quantification of biochemical changes in
265 real-time (**Fig 1C**).

266

267 **T-SLICE culture generates sustained hypoxic gradients**

268 Hypoxia is a hallmark feature of the TME of solid tumors. It results from limited oxygen
269 availability, especially in regions distal to the blood supply[28]. Our simulations predicted that

270 hypoxia would occur most prominently in the middle of the T-SLICE and exhibit relative
271 normoxia at its periphery. To validate this functionally, we identified three concentric zones for
272 analysis: middle (M, 0– 3 mm from center), intermediate (I, 3– 6 mm from center), and periphery
273 (P, 6– 9 mm from center). Using EF5 staining, we measured hypoxia in T-SLICE after 6, 12, 24
274 and 48 h of culture. At all three gap heights tested, increasing time resulted in greater hypoxia
275 among ID8 *Trp53-/-* cells ($p<0.0001$, **Fig 3**); this result was confirmed in two additional second
276 cell lines, MCF7, and HCC1806 (**Supplementary Figs 1 and 2**) and consistent with our
277 simulations (**Fig 1)**. For all cell lines and gap heights tested, EF5 fluorescence intensity was
278 highest in the middle zone of T-SLICE and progressively decreased in the intermediate and
279 peripheral zones. EF5 staining was observed as early as 6h and increased during the 48 h during
280 which we studied cells in T-SLICE for this experiment ($p<0.005$ for all gap heights). Hypoxic
281 gradients were most pronounced with the smallest gap height (300 μm) compared to the larger gap
282 heights, consistent with our prediction of decreasing oxygen availability with restricted diffusion
283 as gap height decreases ($p<0.0001$ at all timepoints).
284

285 **Cell proliferation is diminished in hypoxic regions of T-SLICE**

286 A direct impact of hypoxia in cancer cells is the reduction of proliferation to maintain viability[29].
287 We used the EdU assay to assess whether cellular proliferation is diminished in the hypoxic regions
288 of T-SLICE. After 72h of culture, proliferation of tumor cells in spheroids and fibroblasts was
289 most often observed in the peripheral zone of T-SLICE ($p<0.0001$, **Fig 4 and Supplementary Fig**
290 **3**). Newly divided MCF-7 or HCC1806 cells were not detected in the middle zone, at any gap
291 height. In MCF7 cells, cell proliferation increased with higher gap heights ($p<0.001$), confirming
292 that cellular proliferation and hypoxia are inversely related in T-SLICE.

293 **Cell viability is reduced in the hypoxic regions of T-SLICE**

294 Concurrent with reduced proliferation, loss of cell viability is commonly observed in hypoxic
295 regions of tumors due to deprivation of essential nutrients and oxygen[28]. To examine cellular
296 viability within T-SLICE, we cultured cells for 72h and used Calcein-AM and ethidium
297 homodimer-1 to stain in tandem to identify live (green) and dead (red) cells, respectively **(Fig 5)**.
298 Cell viability remained nearly 100% in the peripheral zone of T-SLICE at all gap heights tested.
299 In ID8 *Trp53*$^{-/-}$ spheroids cultured in 300 µm gap height T-SLICE, cell viability decreased to ~70%
300 and ~20% in the intermediate and middle zones, respectively, but this diminution was nearly
301 completely abrogated when gap heights were raised to 500 µm and 700 µm. Similar cellular
302 viability trends were observed when we instead used MCF-7 cells **(Supplemental Fig 4).**
303

304 **Hypoxia slowed proliferation and cell death in T-SLICE correspond to loss of mitochondrial**
305 **membrane potential**

306 Loss of mitochondrial membrane potential (MMP) is a characteristic early feature of apoptosis and
307 can be brought about by hypoxic stress[29]. MitoView 633 was used to analyze the MMP of cancer
308 cells cultured in T-SLICE for up to 48 h **(Fig 6 and Supplementary Fig 5)**. In both MCF-7 and
309 ID8 *Trp53-/-* spheroids, MMP was significantly diminished in the intermediate zone, and further
310 in the middle zone of T-SLICE compared with the periphery ($p<0.001$). This impact was
311 significantly greater after 48 h ($p<0.001$). Altogether, our results indicate that T-SLICE creates
312 biochemical gradients of hypoxia that correspond to loss of MMP, thereby impacting cellular
313 viability and proliferation, recapitulating the features of native tumors.
314
315

316 **Discussion**

317 Hypoxia is a persistent feature of tumors that establishes much of their heterogeneity and fuels
318 their potential progression and escape from therapeutic interventions[10, 15, 28, 30]. To catalyze cancer
319 research, we created T-SLICE, a simple and effective *in vitro* system that uses a fibroblast
320 monolayer seeded between impermeable top and bottom barriers to establish a cell-driven hypoxic
321 microenvironment. Because the transparent chip is assembled atop a coverslip laden with cells, T-
322 SLICE is fully compatible with live cell imaging. In its simplicity and flexibility, T-SLICE is
323 highly amenable to use in biology laboratories and opens the possibility of testing new therapeutics
324 in a model representative of a native tumor.

325 In our studies, we worked with three tumor cell lines that represented breast and ovarian
326 cancer. With some inter-tumor variation, all tested cell lines generated the same biochemical
327 trends: greater proximity to the middle of T-SLICE corresponded to a reduction in viability,
328 proliferation, and MMP. Compared to cancer models that rely on extrinsically imposed oxygen
329 gradients[31, 32], a cell metabolism-driven gradient is more likely to recapitulate the TME, with
330 flexibility for the investigator to tailor the model to a given tumor histology or characteristics. This
331 is especially valuable given the wide range of oxygen tensions at normoxia within different tissue
332 types[33]. Although we did not directly measure oxygen tension in T-SLICE, EF5 staining, cell
333 viability and proliferation confirmed the generation of hypoxic gradients and their downstream
334 consequences, and their behaviour is consistent with other cell-driven hypoxic cancer models[34, 35].

335 We confirmed that the area of the hypoxic zone in T-SLICE can be increased by reducing the
336 chip gap height. A minimum gap height must be maintained to accommodate spheroids (<150
337 mm), but by increasing the diameter of T-SLICE, one could increase diffusion distances from the
338 periphery to the middle and thus further increase the hypoxic area. By manipulating the gap height

339 and T-SLICE diameters, we can mimic different TMEs and hypoxia levels, making T-SLICE
340 representative of different-sized tumors or at different regions of a tumor with varying distances
341 from blood vessels. By comparison, in spheroid culture, a gold standard practice in cancer research,
342 an increase in hypoxic effect can only be achieved with more cells and larger spheroid diameters
343 which will directly impair the ability to observe cell behaviors within[36]. Using T-SLICE,
344 biochemical gradients can be uncoupled from tissue architecture, so it becomes possible to observe
345 cellular events within a comparable TME to a much larger spheroid.

346 The use of animals as a preclinical screening model has been standard practice in drug
347 development for decades, but the legislation of the FAD Modernization Act 2.0 in 2022[37]
348 encourages alternative model development, including organ-on-a-chip models such as T-SLICE,
349 to improve the predictive power of preclinical studies and lower the cost of drug development.
350 With increasing research into personalized and precision medicine approaches for cancer therapy,
351 there is an urgent need to develop simple, reliable, high-content systems that can be widely adopted
352 by biology research laboratories. Conventional 2-D culture and model organisms have been
353 informative for understanding mechanisms behind disease processes; however, 2-D systems lack
354 a tumor's structural and biochemical characteristics. Model organisms, including xenografted or
355 humanized mice, are excellent tools to study cancer in a complex microenvironment, but lack a
356 human immune system, require extensive workup and monitoring[38], and have much lower
357 throughput compared to *in vitro* platforms, and can be quite heterogeneous.

358 Microfluidic platforms combined with 3-D culture systems allow a small number of explanted
359 tumor, immune, and stromal cells to be grown and studied, but their complex setups make them
360 out of reach for most biology laboratories[39]. Endpoint sample recovery can be challenging such as
361 in sealed microfluidic chips, further impeding their use as a standard model to study cancer

362 biology. In contrast, T-SLICE can be easily assembled using standard cell culture vessels (i.e., 6-
363 well plates), which allows relatively high-throughput tumor studies with continuous monitoring
364 capability in a broadly affordable and feasible manner. The transparency of T-SLICE combined
365 with thin cell layers enables brightfield and fluorescent live-cell imaging. By simply lifting the T-
366 SLICE chip with forceps, selected portions of cells or the entire culture can be harvested for
367 endpoint histologic analysis using standard staining protocol, all without disrupting the overall
368 spatial arrangement of cells.

369 An advantage that T-SLICE shares with microfluidic culture platforms is the low cell
370 number needed to establish culture and biochemical gradients due to the small culture volume. We
371 show that simple adjustments, such as changing the gap height of the chip, have predictable
372 impacts on the hypoxic gradient; this is relevant because oxygen availability varies even within
373 the same tumor[40, 41]. Presently, the hypoxia in T-SLICE is driven primarily by the fibroblast
374 monolayer; however, relative proportions of the tumor, stromal and other cells should be carefully
375 considered and included to reflect specific applications of T-SLICE.

376 In clinical practice, T-SLICE could be used to inform precision therapy. With fewer than
377 100,000 cells, patient "avatars" could be established in a recreated TME. Models using
378 conventional spheroid culture would require several magnitudes more cells and would not be
379 imageable. In T-SLICE, features and interventions can be studied with iteration in adjacent wells
380 of the same plate to test, iterate, and combine treatments to identify the best one for each patient,
381 and on a timeline consistent with informing care[40, 41].

382

383 **Conclusions**

384 T-SLICE is a novel *in vitro* tumor model that captures the biochemical features of the TME.
385 With the shift away from mouse models, and toward the use of miniaturized organ-on-a-

386 chip models for drug development pipelines, there is an unmet need for simple, accessible
387 models. T-SLICE captures key aspects of tumor biochemistry while remaining amenable
388 to techniques and equipment found in standard biology laboratories. By combining features
389 of existing *in vitro* technologies, such as spheroid culture, and subjecting them to an
390 environment that intrinsically imposes TME features, T-SLICE can meet the demand for
391 accessible tumor model systems.

392 **Author contributions**

393 The T-SLICE model and study was conceptualized by MPT, ND, AS, JEB, and BML;
394 experiments were designed, conducted, and validated by MPT, ND, and AS. Data analysis was
395 conducted by MPT, ND, AS, JEB, and BML. The manuscript was written by MPT, ND, AS,
396 JEB, and BML, reviewed, edited, and approved by all authors.

397

398 **Acknowledgements**

399 The authors thank Ms. Sarah Nersesian and Dr. Naeimeh Jafari for technical assistance and
400 discussions on T-SLICE development. MPT and ND are trainees in the Cancer Research Training
401 Program of the Beatrice Hunter Cancer Research Institute, with funds for MPT previously
402 provided by the Bruce and Dorothy Rosetti Endowment through the Dalhousie Medical Research
403 Foundation and funds for ND previously provided by the Helyer/Williams Studentship. MPT is
404 funded by a CIHR Canadian Graduate Scholarship - Doctoral and a Scotia Scholars Scholarship.
405 ND was supported by a Canadian Graduate Scholarship (Masters; NSERC) and a Genomics in
406 Medicine Scholarship through the Dalhousie Medical Research Foundation. JEB is the Dalhousie
407 Medical Research Foundation Cameron Cancer Scientist. We acknowledge the support of the
408 Government of Canada's New Frontiers in Research Fund (NFRF), [NFRFE2019-00415] for

409 funding this research. Funding was additionally provided by Health Canada to Ovarian Cancer
410 Canada in support of the OvCAN research initiative. We thank Dr. Madhuri Koti (Queen's
411 University) for the ID8-Trp53$^{-/-}$ cell line.

412 **Conflicts of interest**

413 There are no conflicts to declare.

414 **Data availability**

415 All data generated or analysed during this study are included in this published article and
416 supplementary data.
417

References

1. B. Emon, J. Bauer, Y. Jain, B. Jung and T. Saif, *Comput Struct Biotechnol J*, 2018, **16**, 279-287.
2. F. R. Balkwill, M. Capasso and T. Hagemann, *Journal of Cell Science*, 2012, **125**, 5591-5596.
3. G. Imparato, F. Urciuolo and P. A. Netti, *International Materials Reviews*, 2015, **60**, 297-311.
4. Y. Liu and H. Lu, *Curr Opin Biotechnol*, 2016, **39**, 215-220.
5. J. Wu, H. Fang, J. Zhang and S. Yan, *Journal of Nanobiotechnology*, 2023, **21**, 85.
6. G. Velve-Casquillas, M. Le Berre, M. Piel and P. T. Tran, *Nano Today*, 2010, **5**, 28-47.
7. Y. Li, L. Zhao and X. F. Li, *Technol Cancer Res Treat*, 2021, **20**, 15330338211036304.
8. G. Chen, K. Wu, H. Li, D. Xia and T. He, *Front Oncol*, 2022, **12**, 961637.
9. Z. Chen, F. Han, Y. Du, H. Shi and W. Zhou, *Signal Transduction and Targeted Therapy*, 2023, **8**, 70.
10. V. Petrova, M. Annicchiarico-Petruzzelli, G. Melino and I. Amelio, *Oncogenesis*, 2018, **7**, 10.
11. X. Jing, F. Yang, C. Shao, K. Wei, M. Xie, H. Shen and Y. Shu, *Mol Cancer*, 2019, **18**, 157.
12. S. Romero-Garcia, J. S. Lopez-Gonzalez, J. L. Báez-Viveros, D. Aguilar-Cazares and H. Prado-Garcia, *Cancer Biol Ther*, 2011, **12**, 939-948.
13. C. Navarro, Á. Ortega, R. Santeliz, B. Garrido, M. Chacín, N. Galban, I. Vera, J. B. De Sanctis and V. Bermúdez, *Pharmaceutics*, 2022, **14**.
14. C. Carmona-Fontaine, M. Deforet, L. Akkari, C. B. Thompson, J. A. Joyce and J. B. Xavier, *Proceedings of the National Academy of Sciences*, 2017, **114**, 2934-2939.
15. R. Abou Khouzam, K. Brodaczewska, A. Filipiak, N. A. Zeinelabdin, S. Buart, C. Szczylik, C. Kieda and S. Chouaib, *Front Immunol*, 2020, **11**, 613114.
16. C. H. Wong, K. W. Siah and A. W. Lo, *Biostatistics*, 2018, **20**, 366-366.
17. F. Spagnolo, A. Boutros, F. Cecchi, E. Croce, E. T. Tanda and P. Queirolo, *BMC Cancer*, 2021, **21**, 425.
18. T. K. Ngan Ngo, C.-H. Kuo and T.-Y. Tu, *Biomicrofluidics*, 2023, **17**.
19. H. Mollica, Y. J. Teo, A. S. M. Tan, D. Z. M. Tan, P. Decuzzi, A. Pavesi and G. Adriani, *Biomaterials Science*, 2021, **9**, 7420-7431.
20. M. Virumbrales-Muñoz, J. Chen, J. Ayuso, M. Lee, E. J. Abel and D. J. Beebe, *Lab on a Chip*, 2020, **20**, 4420-4432.
21. D. M. Cochran, D. Fukumura, M. Ancukiewicz, P. Carmeliet and R. K. Jain, *Annals of Biomedical Engineering*, 2006, **34**, 1247-1258.
22. J. M. Oh, H. M. Begum, Y. L. Liu, Y. Ren and K. Shen, *ACS Biomaterials Science & Engineering*, 2022, **8**, 3107-3121.
23. G. Corredor, X. Wang, Y. Zhou, C. Lu, P. Fu, K. Syrigos, D. L. Rimm, M. Yang, E. Romero, K. A. Schalper, V. Velcheti and A. Madabhushi, *Clin Cancer Res*, 2019, **25**, 1526-1534.

24. D. E. Cohn, A. Forder, E. A. Marshall, E. A. Vucic, G. L. Stewart, K. Noureddine, W. W. Lockwood, C. E. MacAulay, M. Guillaud and W. L. Lam, *Front Immunol*, 2023, **14**, 1275890.
25. S. Nersesian, R. J. Arseneau, J. P. Mejia, S. N. Lee, L. P. Westhaver, N. W. Griffiths, S. R. Grantham, L. Meunier, L. Communal, A. Mukherjee, A.-M. Mes-Masson, T. Arnason, B. H. Nelson and J. E. Boudreau, *Frontiers in Immunology*, 2024, **14**.
26. F. Katou, H. Ohtani, Y. Watanabe, T. Nakayama, O. Yoshie and K. Hashimoto, *Cancer Research*, 2007, **67**, 11195-11201.
27. C. H. Cho, J. Park, D. Nagrath, A. W. Tilles, F. Berthiaume, M. Toner and M. L. Yarmush, *Biotechnol Bioeng*, 2007, **97**, 188-199.
28. V. Bhandari, C. Hoey, L. Y. Liu, E. Lalonde, J. Ray, J. Livingstone, R. Lesurf, Y. J. Shiah, T. Vujcic, X. Huang, S. M. G. Espiritu, L. E. Heisler, F. Yousif, V. Huang, T. N. Yamaguchi, C. Q. Yao, V. Y. Sabelnykova, M. Fraser, M. L. K. Chua, T. van der Kwast, S. K. Liu, P. C. Boutros and R. G. Bristow, *Nat Genet*, 2019, **51**, 308-318.
29. X. Zhao, L. Liu, R. Li, X. Wei, W. Luan, P. Liu and J. Zhao, *Med Sci Monit*, 2018, **24**, 8722-8733.
30. W. Zeng, P. Liu, W. Pan, S. R. Singh and Y. Wei, *Cancer Lett*, 2015, **356**, 263-267.
31. L. Orcheston-Findlay, A. Hashemi, A. Garrill and V. Nock, *Microelectronic Engineering*, 2018, **195**, 107-113.
32. H. Nam, K. Funamoto and J. S. Jeon, *Biomicrofluidics*, 2020, **14**, 044107.
33. A. Carreau, B. El Hafny-Rahbi, A. Matejuk, C. Grillon and C. Kieda, *J Cell Mol Med*, 2011, **15**, 1239-1253.
34. B. Mosadegh, M. R. Lockett, K. T. Minn, K. A. Simon, K. Gilbert, S. Hillier, D. Newsome, H. Li, A. B. Hall, D. M. Boucher, B. K. Eustace and G. M. Whitesides, *Biomaterials*, 2015, **52**, 262-271.
35. D. Rodenhizer, T. Dean, B. Xu, D. Cojocari and A. P. McGuigan, *Nature Protocols*, 2018, **13**, 1917-1957.
36. M. Roy, C. Alix, A. Bouakaz, S. Serrière and J. M. Escoffre, *Pharmaceutics*, 2023, **15**.
37. P.-J. H. Zushin, S. Mukherjee and J. C. Wu, *The Journal of Clinical Investigation*, 2023, **133**.
38. N. C. Walsh, L. L. Kenney, S. Jangalwe, K. E. Aryee, D. L. Greiner, M. A. Brehm and L. D. Shultz, *Annu Rev Pathol*, 2017, **12**, 187-215.
39. J. H. Hammel, S. R. Cook, M. C. Belanger, J. M. Munson and R. R. Pompano, *Annu Rev Biomed Eng*, 2021, **23**, 461-491.
40. G. J. Yoshida, *J Hematol Oncol*, 2020, **13**, 4.
41. P. Voabil, M. de Bruijn, L. M. Roelofsen, S. H. Hendriks, S. Brokamp, M. van den Braber, A. Broeks, J. Sanders, P. Herzig, A. Zippelius, C. U. Blank, K. J. Hartemink, K. Monkhorst, J. B. A. G. Haanen, T. N. Schumacher and D. S. Thommen, *Nature Medicine*, 2021, **27**, 1250-1261.

499 **Figures**

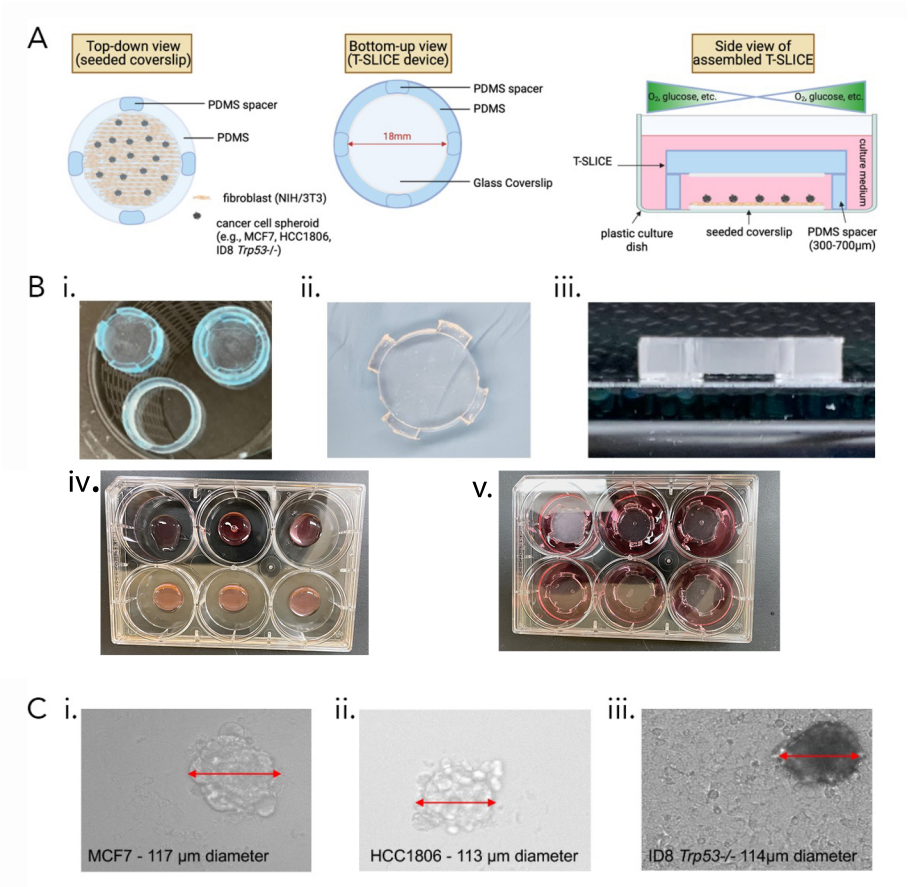

500

501 **Fig 1: T-SLICE Schematic, Design & Assembly. (A)** Top, bottom and side-view schematic of
502 T-SLICE demonstrating the placement of chips and resulting biochemical gradients. (B)
503 photograph of (i) two-part T-SLICE mold (shown both assembled, top right and in the component
504 ring and insert pieces (bottom and top left); (ii) top-down and (iii) side view of assembled T-
505 SLICE; (iv) Top-down view of T-SLICE cultures assembled in a six-well plate without and (v)
506 with a T-SLICE chip added on top. (C) photographs depicting tumor cell line spheroids atop
507 fibroblast monolayers imaged through a T-SLICE chip: (i) MCF7; (ii) HCC1806; (iii) ID8 *Trp53*$^{-}$
508 $^{/-}$.

509

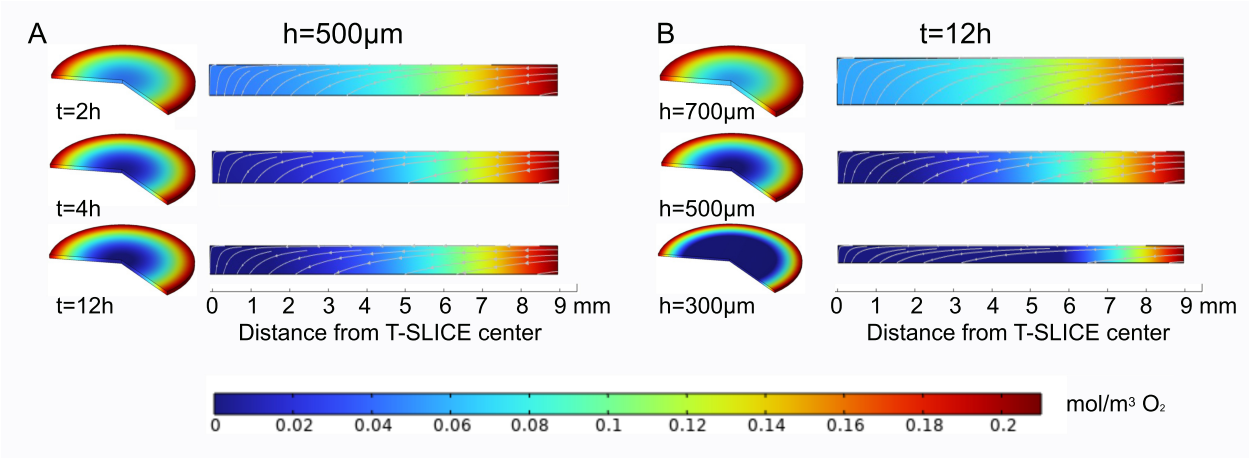

Fig 2: Computational Simulations of Oxygen Gradients in T-SLICE. Expected radial oxygen concentration gradient within the T-SLICE as a function of (A) time (500 mm gap height) and (B) gap heights (at 12 hours). Oxygen diffusion through the culture media under T-SLICE was simulated using COMSOL Multiphysics, where a time-dependent transport of diluted species study was constructed. A rectangle was created in the 2D axisymmetric space dimension with the left side of the rectangle as the axis of symmetry. The length was set to the radius of the T-SLICE (9 mm), and the height was varied to match the different gap heights (300, 500, 700 mm). The material in the space between the top and bottom was modelled as water at 37 °C to simulate culture media: the diffusion coefficient was set to 3 x 10-9 m^2/s, and the initial concentration of oxygen was set to the dissolved oxygen saturation point of 6.7 mg/L (0.21 mol/m^3) based on literature values. Data are presented as a heatmap from low (0 mol/m^2, dark blue) to high (0.2 mol/m^2, dark red) oxygen concentrations.

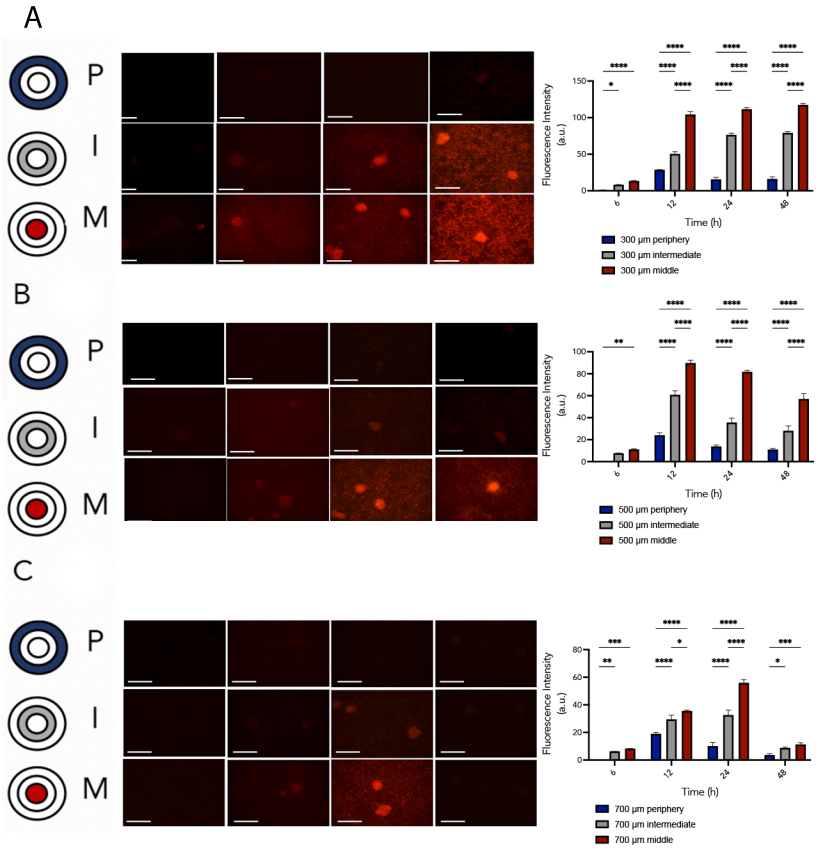

Fig 3: T-SLICE generates hypoxic gradients from the periphery to the center. *ID8 Trp53-/-* spheroids were seeded atop a fibroblast monolayer for 6, 12, 24 or 28h in a T-SLICE chip with EF5-containing media. Thereafter, cells were fixed and stained with anti-EF5 to ascertain hypoxic responses (A-C): photographs and fluorescence quantifications; (D-E) co-cultures under T-SLICE without the EF5 compound. P: periphery, I: intermediate, M: middle. A.u: arbitrary units. Scale bars represent 275mm. Data are representative of three technical replicates with measurements of fluorescence intensity in three fields of view for each zone ($p<0.0001$, error bars represent standard deviation (SD).

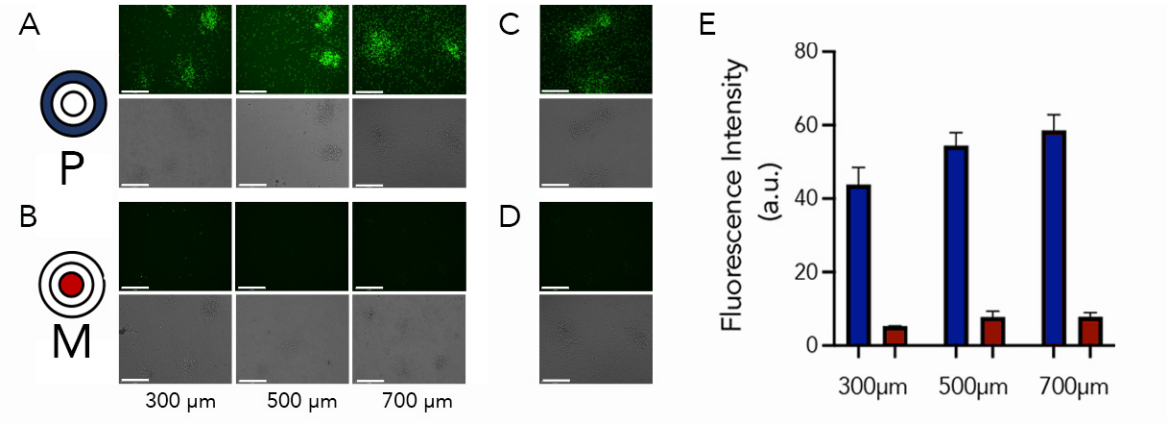

Fig 4: Cellular proliferation is halted in the middle region of T-SLICE. MCF-7 cells were seeded on a fibroblast monolayer in T-SLICE in the presence of EDU. After 72h incubation, cellular proliferation (EDU incorporation) was ascertained by fluorescence microscopy. (A) peripheral zone; (B) Middle zone; C) No T-SLICE control; D) unstained control; (E) quantification of fluorescence. a.u., Arbitrary units. Blue bars represent quantification from the peripheral zone; red bars represent quantification from the middle zone. Scale bars represent 275mm. Data are representative of three technical replicates with measurements of fluorescence intensity in three fields of view for each zone ($p<0.0001$, error bars represent SD).

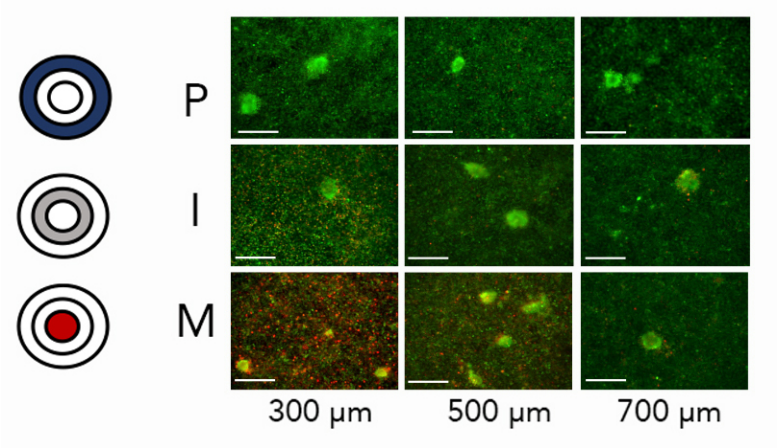

Fig 5: Cellular viability is lost in the most hypoxic regions of T-SLICE. ID8-Trp53$^{-/-}$ spheroids were cultured in T-SLICE on a fibroblast monolayer for 72h, then stained with Calcein-AM and ethidium homodimer to visualize cell viability. Images are representative of three technical replicates and three fields of view for each T-SLICE zone. P, periphery; I, intermediate; M, middle.

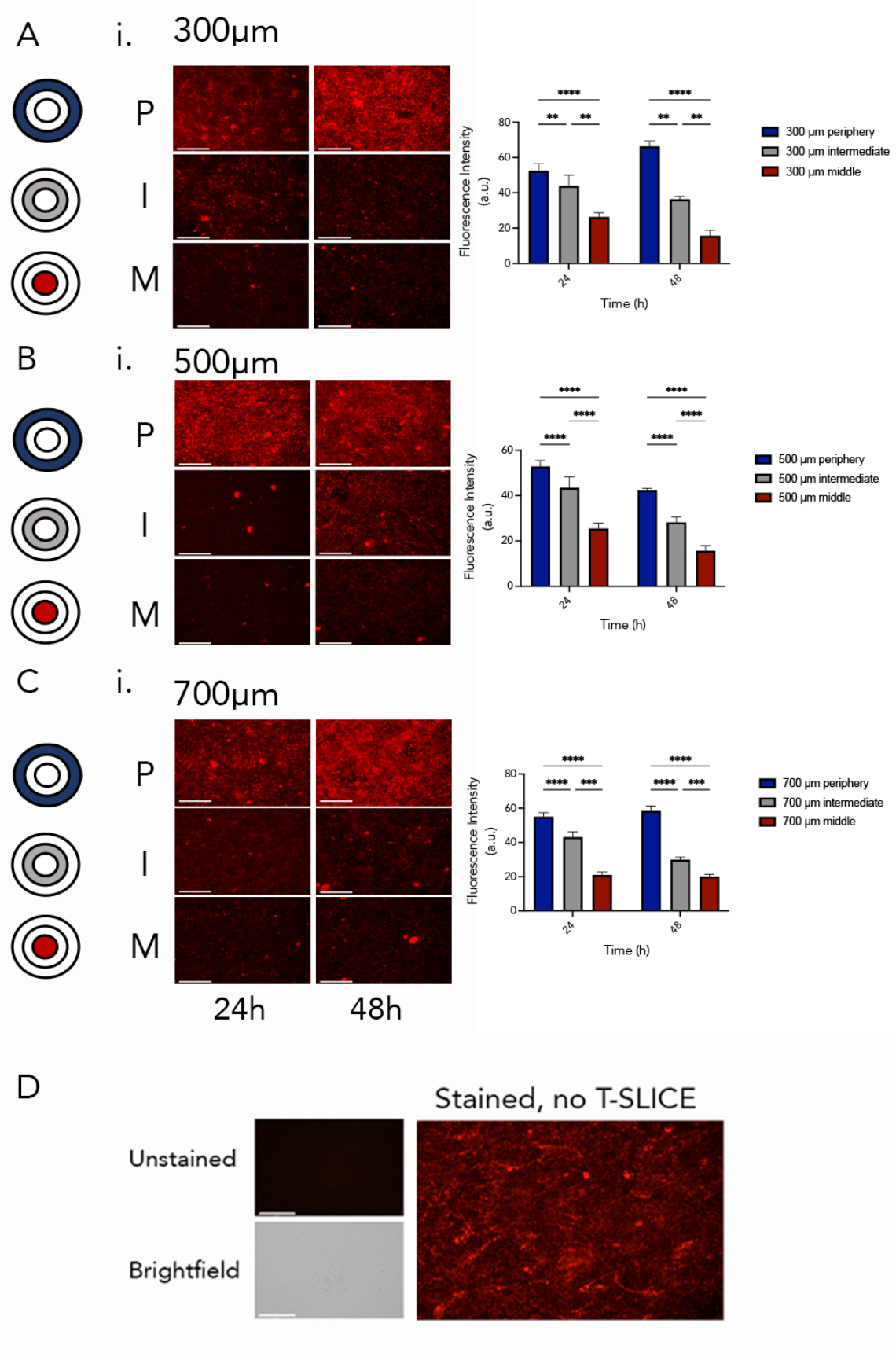
A
i.
300µm
P
I
M
Fluorescence Intensity (a.u.)
Time (h)
24
48
300 µm periphery
300 µm intermediate
300 µm middle
B
i.
500µm
500 µm periphery
500 µm intermediate
500 µm middle
C
i.
700µm
700 µm periphery
700 µm intermediate
700 µm middle
24h
48h
D
Stained, no T-SLICE
Unstained
Brightfield

551

552 **Fig 6: Mitochondrial membrane potential is reduced in T-SLICE.** MMP was measured using
553 MitoView 633 staining after 24 or 48h in MCF7 cells. Significant diminishment was observed in
554 the intermediate and middle zones compared to the periphery ($p<0.001$) with greater impact after
555 48h ($p<0.001$). (A-C) each of the 300, 500 and 700 μM gap heights were tested. (i) representative
556 images; and (ii) quantification are shown. (D) controls included unstained cells in T-SLICE, and
557 stained cells with no T-SLICE. P, periphery (blue); M, middle (grey); I, intermediate (red); a.u.,
558 Arbitrary units. Scale bars represent 275mm. Data are representative of three technical replicates
559 with measurements of fluorescence intensity in three fields of view for each zone ($p<0.001$ after
560 24h, $p<0.0001$ after 48h, error bars represent SD).
561